Acta Pharmaceutica Sinica B 2025;15(5):2468−2479

Chinese Pharmaceutical Association
Institute of Materia Medica, Chinese Academy of Medical Sciences

Acta Pharmaceutica Sinica B

www.elsevier.com/locate/apsb
www.sciencedirect.com

ORIGINAL ARTICLE

Structural insights into the binding modes of lanreotide and pasireotide with somatostatin receptor 1

Zicheng Zeng[a,†], Qiwen Liao[a,†], Shiyi Gan[a,†], Xinyu Li[a], Tiantian Xiong[a], Lezhi Xu[a], Dan Li[a], Yunlu Jiang[b], Jing Chen[b,e,*], Richard Ye[a,c,d,*], Yang Du[a,c,*], Thiansze Wong[a,*]

[a]*Kobilka Institute of Innovative Drug Discovery, School of Medicine, the Chinese University of Hong Kong, Shenzhen 518172, China*
[b]*Neurobiology Key Laboratory of Jining Medical University, Jining 272067, China*
[c]*Shenzhen Futian Biomedical Innovation R&D Center, the Chinese University of Hong Kong, Shenzhen 518033, China*
[d]*The Second Affiliated Hospital, School of Medicine, the Chinese University of Hong Kong, Shenzhen 518172, China*
[e]*Warwick Medical School, University of Warwick, Coventry CV47AL, United Kingdom*

Received 25 December 2024; received in revised form 2 March 2025; accepted 3 March 2025

KEY WORDS

G protein-coupled receptor;
Membrane protein;
Somatostatin receptor 1;
SSTR1;
Somatostatin analog;
Lanreotide;
Pasireotide;
Cryo-EM;
Structural biology

Abstract Somatostatin receptor 1 (SSTR1) is a crucial therapeutic target for various neuroendocrine and oncological disorders. Current SSTR1-targeted treatments, including the first-generation somatostatin analog lanreotide (Lan) and the second-generation analog pasireotide (Pas), show promise but encounter challenges related to selectivity and efficacy. This study presents high-resolution cryo-electron microscopy structures of SSTR1 complexed with Lan or Pas, revealing the distinct mechanisms of ligand-binding and activation. These structures illustrate unique conformational changes in the SSTR1 orthosteric pocket induced by each ligand, which are critical for receptor activation and ligand selectivity. Combined with the biochemical assays and molecular dynamics simulations, our results provide a comparative analysis of binding characteristics within the SSTR family, highlighting subtle differences in SSTR1 activation by Lan and Pas. These insights pave the way for designing next-generation therapies with enhanced efficacy and reduced side effects through improved receptor subtype selectivity.

*Corresponding authors.
E-mail addresses: thiansze@gmail.com (Thiansze Wong), yangdu@cuhk.edu.cn (Yang Du), richardye@cuhk.edu.cn (Richard Ye), Jing.Chen@warwick.ac.uk (Jing Chen).
[†]These authors made equal contributions to this work.
Peer review under the responsibility of Chinese Pharmaceutical Association and Institute of Materia Medica, Chinese Academy of Medical Sciences.

https://doi.org/10.1016/j.apsb.2025.03.043

1. Introduction

Somatostatin (SST) is a cyclic peptide the body produces to control hormone release. It is secreted by the central nervous system, gastrointestinal tract, and the islets of Langerhans of the pancreas. Endogenous SST has 2 active forms that vary in constituent amino acids: SST14 and SST28[1]. By activating somatostatin receptors (SSTR), SST can inhibit the secretion of various hormones such as growth hormone, corticotropin, and ghrelin. Further, SST regulates glucose metabolism by controlling the pancreatic release of insulin and glucagon. The agonistic effect of SST can affect innate and adaptative immune responses *via* controlling immune cell proliferation and cytokine release[2]. Further, SST can inhibit cell cycle progression and DNA synthesis by stimulating the non-transmembrane tyrosine phosphatase SHP-1 and SHP-2[3,4].

SSTR belongs to class A GPCRs, which are widely expressed throughout the human body, with 5 distinct subtypes identified in mammals: SSTR1, SSTR2A/B, SSTR3, SSTR4, and SSTR5[5]. When bound to SST, SSTR1 couples with Gi proteins, triggering downstream signaling pathways, which are essential for hormone expression and release[6].

Heterogeneous SSTR expression is observed in neuroendocrine tumors (NET)[7]. Thus, targeting SSTR with recombinant SST or somatostatin analogs (SSA) is an attractive therapeutic strategy. Theoretically, recombinant SST has an anti-proliferative effect on cancers that express high levels of SSTR. However, the short half-life of endogenous SST in circulation limits its clinical utility[8]. As a result, synthetic SSA with greater stability are being developed for therapeutic use. Currently, there is no selective SSA. All synthetic SST analogs developed so far can bind to all five SSTR subtypes. Their therapeutic effects are primarily mediated through SSTR2 and SSTR5. Lanreotide (Lan) is one of the first-generation SSA designed for the treatment of acromegaly as the acromegalic somatotroph cells showed frequently high expression of SSTR2[9]. The second-generation somatostatin analog, pasireotide (Pas), preferentially binds to SSTR5 than SSTR2[10].

SSTR2 and SSTR5 are commonly overexpressed in various human tumors, making them frequent targets for cancer therapies. In contrast, SSTR1 exhibits a unique expression pattern, occurring preferentially in specific tumor types. Notably, ductal pancreatic carcinomas and primary hormone-sensitive prostate cancers show a higher prevalence of SSTR1 expression[11]. This distinct distribution of SSTR1 in certain malignancies highlights its potential as a specific therapeutic target for these particular cancer types. While synthetic SSA like Lan and Pas can bind to SSTR1, their affinity is significantly weaker compared to the endogenous SST14[12]. Specifically, Lan affinity to SSTR1 is nearly 200 times lower than that of SST14, demonstrating a substantial reduction in binding strength. Pas, although showing improved affinity for SSTR1 compared to Lan, still exhibits a tenfold decrease in binding strength relative to SST14[12]. This marked difference in affinity highlights a therapeutic gap in our current cancer treatment regime. Thus, developing a new SSA that can selectively and potently target SSTR1 has become a pressing need.

In this study, we utilized cryo-electron microscopy to elucidate the structures of SSTR1 in complex with Lan or Pas. These structural insights are vital for comprehending the unique drug-binding properties of SSTR1, potentially guiding the discovery of novel drugs for cancers that predominantly express SSTR1. Furthermore, the atomic-level details will offer valuable information to enhance current SSTR-targeted therapies and may improve selectivity for specific cancer types.

2. Materials and methods

2.1. Constructs of SSTR1, DNGi, Gβ1, Gγ2 and scFv16

The human SSTR1 gene was synthesized by Sangon Biotech (Shanghai) Co., Ltd., and cloned into the pFastbac1 vector (Gibco), which contains an N-terminal Flag tag and a C-terminal 10xHis tag, with an HRC 3C protease cleavage site sequence inserted between the tag and the protein sequence. To enhance expression levels, a bacteriorhodopsin-like protein (BRIL) sequence from the tropical sponge Lantern bell, a homolog of bacteriorhodopsin, was used at the N-terminus. A dominant-negative human Gαi subunit (DNGi) and scFv16 were cloned into the pFastbac1 vector (Gibco), while the human Gβ1 and human Gγ2 subunits were cloned into the pFastBac-Dual vector (Gibco). All proteins were expressed using the cloned isolate sf9 cells derived from the parental *Spodoptera frugiperda* cell line.

2.2. Expression and purification of SSTR1−DNGi complex

The Bac-to-Bac system was utilized to express the SSTR1−DNGi complex. Plasmids containing SSTR1 and the three G protein subunits were transformed into DH10Bac cells, which harbor a baculovirus shuttle vector and a helper plasmid that facilitate site-specific recombination of pFastBac with bMON14272 to generate high-molecular-weight bacmids. Subsequently, the bacmid was transfected into sf9 cells using FuGENE HD Transfection Reagent (Promega, Madison, WI, USA), and P0 virus was harvested after 96 h of culture. 100 μL of each of the 3 P0 viruses were then inoculated into 50 mL of sf9 cells at a density of 2 million cells/mL and cultured for 60 h to harvest the P1 virus. The purified P1 viruses of SSTR1, DNGi, and Gβ1/Gγ2 were co-expressed at a volume ratio of 10:10:1 in 2 L of sf9 cells at a concentration of 4×10^6 cells/mL, and cells were collected 48 h later.

The harvested cells were snap-frozen in liquid nitrogen and lysed in a buffer containing 10 mmol/L HEPES pH 7.4, 1 mmol/L EDTA, 1 mg/mL iodoacetamide, 1 mmol/L Lan/Pas. After centrifugation at 39,191 × *g* for 30 min, the cell membrane pellet was collected. The membranes were then resuspended in a buffer formulated with 20 mmol/L HEPES pH 7.4, 100 mmol/L NaCl, 2.5 μg/mL leupeptin, 0.16 mg/mL benzamidine, 1 mg/mL iodoacetamide, 10 mmol/L $CaCl_2$, 10% glycerol, 10% *n*-dodecyl-β-D-maltopyranoside (DDM), and 1 mmol/L Lan/Pas adjusted to pH 7.0, and incubated at 4 °C for 2 h. After centrifugation at 48,384 × *g*, the supernatant containing the SSTR1−DNGi

complex was incubated with anti-FLAG M1 affinity resin at 4 °C for 1 h.

After incubation, the mixture was allowed to stand for 5 min before being centrifuged at 484×*g* for 5 min at 4 °C to collect the resin bound to the SSTR1−DNGi complex. A gradient buffer exchange was performed using Buffer A containing 20 mmol/L HEPES pH 7.0, 100 mmol/L NaCl, 1% *n*-dodecyl-*β*-D-maltopyranoside, 0.1% cholesterol hemisuccinate (CHS), 2 mmol/L $CaCl_2$, and 1 mmol/L Lan/Pas and Buffer B containing 20 mmol/L HEPES pH 7.0, 100 mmol/L NaCl, 1% lauryl maltose neopentyl glycol (LMNG), 0.1% CHS, 2 mmol/L $CaCl_2$, and 1 mmol/L Lan/Pas. The chromatography column was subsequently washed with 20 mmol/L HEPES pH 7.0, 100 mmol/L NaCl, 0.1% LMNG, 0.01% CHS, 0.01% glyco-diosgenin (GDN), 2 mmol/L $CaCl_2$, and 1 mmol/L Lan/Pas. Elution was performed using a buffer composed of 20 mmol/L HEPES pH 7.0, 100 mmol/L NaCl, 0.003% LMNG, 0.001% GDN, 0.004% CHS, 1 mmol/L Lan/Pas, 200 μmol/L flag peptide, and 5 mmol/L EDTA.

The eluate was incubated with 20 μL of 10 mg/mL scFv16 at 4 °C for 12 h, followed by size-exclusion chromatography using a Superose 6 increase 10/300 column GL (Cytiva, Uppsala, Sweden) with a running buffer of 20 mmol/L HEPES pH 7.0, 100 mmol/L NaCl, 0.003% LMNG, 0.001% GDN, 0.004% CHS, and 1 mmol/L Lan/Pas to separate the complex from unassembled proteins. The protein obtained from chromatographic purification was concentrated to 5 mg/mL for cryo-EM sample preparation.

2.3. Cryo-EM sample preparation and data acquisition

A 3 μL aliquot of the SSTR1−DNGi−Lan−scFv16 or SSTR1−DNGi−Pas−scFv16 complex was applied to gold grids (UltraAuFoil/QuantiFoil, 300 mesh, R1.2/1.3, Quantifoil Micro Tools GmbH, Jena, Germany) or amorphous alloy grids (300 mesh, R1.2/1.3, Zhenjiang Lehua Electronic Technology Co., Ltd., Zhenjiang, China), which had been glow-discharged with air for 40 s at 15 mA using the Glow Discharge Cleaning System (easiGlow, Ted Pella, Redding, CA, USA). The grids were then blotted for 4 s with a blotting force of 0 using the Vitrobot Mark IV (ThermoFisher Scientific) and rapidly plunged into liquid ethane. The prepared grids were stored in liquid nitrogen. Cryo-EM imaging was performed using a 300 kV Titan Krios Gi3 microscope at the Kobilka Cryo-EM Center, The Chinese University of Hong Kong, Shenzhen, China. Data collection for SSTR1−Lan was conducted at 0.83 Å, and for SSTR1-Pas at 0.85 Å, with image data recorded using the SerialEM5 software. The defocus value range for the cryo-EM used in this study was from −1.0 to −2.0 μm. The electron dose of SSTR1-Pas was 53.60 e/Å^2 and SSTR1−Lan was 53.50 e/Å^2.

2.4. Cryo-EM data processing

The cryo-EM data was analyzed by cryoSPARC (v4.4.1). For SSTR1−Pas, a total of 3250 movies were imported. Following patch motion correction and CTF estimation, 3186 micrographs were generated, yielding 2,969,804 particles. After multiple rounds of 2D classification, 1,413,155 particles were selected for 3D classification. This process resulted in a map with a resolution of 2.79 Å from 722,906 particles, as shown in Supporting Information Fig. S1. For SSTR1−Lan, 3951 movies were imported and processed using a similar workflow as SSTR1−Pas. After five rounds of 2D classification, 1,406,862 particles were taken forward for 3D classification. Additionally, we applied local refinement to further improve the results. A final map with a resolution of 3.37 Å was obtained from 217,201 particles, as shown in Supporting Information Fig. S2.

2.5. Model building and refinement

The atomic model was built on the cryo-EM density map, utilizing the available structures of DNGi from SSTR2−SST14 (PDB 7XMR), Gβ1, Gγ2, scFv16 from SSTR2−Lan (PDB 7T10), and the AlphaFold-predicted SSTR1 structure. Firstly, the initial models were docked into the electron density maps using UCSF ChimeraX, adjusting their positions to align with the actual densities. Subsequently, the models were modified and adjusted using WinCoot (v0.9.8.95). The models were then refined in Phenix (v1.20.1−4487) to optimize topology and spatial conformation. After validation using RCSB PDB MolProbity, the refined structural files and electron density maps were deposited in the Protein Data Bank (PDB) and the Electron Microscopy Data Bank (EMDB). The SSTR1−Pas and SSTR1−Lan structures are available under PDB codes 9IK8 and 9IK9, with corresponding electron density maps deposited in the EMDB under accession codes EMD-60650 and EMD-60651.

2.6. Molecular docking

To determine the precise binding conformation of Lan to SSTR1, we performed molecular docking using the Glide module in Schrödinger Maestro (v13.8). We first prepared the receptor protein using the Protein Preparation Wizard, which was employed to add missing side chains and loops and to adjust protonation states. We then neutralized Lan using the LigPrep tool and defined a docking grid within the receptor's binding pocket. After completing these preparations, we conducted the docking analysis and selected the conformations (Conf) with the highest docking scores.

2.7. Molecular dynamics simulations

Molecular dynamics (MD) simulations were performed for conf1-bound, conf2-bound, and conf3-bound SSTR1 to evaluate the stability of different conformations binding to SSTR1. The membrane builder module in CHARMM-GUI server[13] was used to prepare the simulation inputs. The ligand−protein complexes were embedded into a membrane bilayer composed of POPC molecules, and the position was based on the OPM database[14]. Then, the complex was solvated with TIP3P solvent and 0.15 mol/L NaCl. CHARMM36 forcefield[15] was used for the protein, lipids, and ions. CHARMM general force field (CGenFF)[16] was used for agonists. All MD simulations are performed using GROMACS-2019.4[17]. Energy minimization was firstly performed on prepared systems for 5000 steps by the steepest descent algorithm, and then a 125 ps NVT simulation at 310 K was generated for the solvent equilibration using the Berendsen thermostat with heavy atoms restrained at 10.0 kcal/mol·Å^2. The equilibration was processed for an additional 5 cycles, during which the harmonic restraints were 5.0, 2.5, 1.0, 0.5, and 0.1 kcal/mol·Å^2. The equilibration was applied at 310 K and 1 atm for 1 ns in NPT ensemble, using the Berendsen thermostat and barostat. Finally, the production simulations were run at 310 K and 1 atm in the NPT ensemble for 500 ns with a time step of 2 fs, using the Nosé−Hoover Langevin thermostat and the Parrinello−Rahman barostat. A cutoff of 12 Å was used

for the van der Waals and short-range electrostatic interactions. Long-range electrostatic interactions were treated by the particle mesh Ewald algorithm[18]. The covalent bonds containing hydrogen atoms were constrained using the LINCS algorithm[19]. Three independent MD simulations were conducted for each of the 3 systems. The trajectories were recorded at 10 ps intervals and subsequently analyzed using the MDAnalysis library[20]. Root Mean Square Deviation (RMSD) calculations were performed using the Cα atoms of the all-helical regions for alignment, and the heavy atoms of the ligand for the RMSD evaluation. The binding-free MM/PBSA method in gmx_MMPBSA[21] was used to calculate the binding-free energy. For each trajectory, the last 400 ns of each simulation will be used. The lower RMSD and more negative binding free energy indicate better maintenance of structural integrity and a more stable complex with the receptor.

2.8. SSTR1 expression level determination

HEK 293T cells were seeded in a 24-well plate one day before transfection. Plasmid transfection was performed with pcDNA3.1 vector encoding SSTR1 or its mutants. After 24 h incubation, the transfected cells were collected and resuspended in HBSS buffer containing 5% BSA for 30 min on ice. The cells were then incubated on ice for 30 min with DYKDDDDK Epitope Tag Alexa Fluor 488-conjugated antibody (Cat #IC8529G, R&D SYSTEMS, Minneapolis, MN, USA). The fluorescence associated with the antibody−receptor complex on the cell surface was quantified by flow cytometry (CytoFLEX, Bechman Couter, Brea, CA, USA).

2.9. cAMP inhibition assay

A Förster resonance energy transfer (FRET)-based Exchange protein directly activated by cAMP (Epac) sensor was used to measure cellular cAMP levels[22]. The sensor was combined by the donor mTurquoise2 N-terminally fused to Epac-SH187, and the double acceptor tandem of cp173Venus was fused to the C-terminus[23]. The Epac sensor (mTurquoise2−Epac−SH187 −cp173Venus−cp173Venus) described above was cloned to the pcDNA3.1 vector.

HEK 293T cells were seeded in a 6-well plate 1 day before transfection. Plasmid transfection was performed with a mixture of pcDNA3.1 vector encoding SSTR1 or its mutant and pcDNA3.1 vector encoding Epac sensor with a ratio of 1:2. After 48 h incubation, the transfected cells were collected and resuspended in HBSS buffer containing 5 mmol/L HEPES, 0.5 mmol/L IBMX and 0.1% BSA. Next, the cells (50 μL) were added to 96-well black clear bottom plate at 50,000 cells per well, and 25 μL different concentrations of the agonists (Pas or Lan) were added to the plate and incubated at 37 °C for 30 min. Then 25 μL of forskolin were added to the plate at a final concentration of 2.5 μmol/L and incubated at 37 °C for 30 min. The intracellular cAMP level was measured using a FlexStation III (Molecular Devices, San Jose, CA, USA) by detecting fluorescence emission intensity at 485 and 535 nm following excitation at 430 nm. The FRET signal was calculated as the normalized ratio of fluorescence emission at 485 nm divided by emission at 535 nm.

2.10. Statistical analysis

The collected data were analyzed with Prism 10 (GraphPad, San Diego, CA, USA). For generating dose−response curves, the calculated signals were fitted to a three-parameter sigmoidal concentration−response curve. Data points were presented as mean ± standard error of mean (SEM) of maximal luminescence ratio, and maximal cAMP levels of dose−response curves of Gi protein dissociation, and cAMP inhibition, respectively. At the same time, the parameters span, which equals to Top deducted by Bottom, was considered as efficacies. The calculated potencies and efficacies were normalized to those of the wild-type (WT) SSTR1 performed in parallel. One-way analysis of variance (ANOVA) with Dunnett's correction was applied in multiple comparisons to the WT group. The *P*-values less than 0.05 were considered statistically significant.

3. Results

3.1. Cryo-EM structures of SSTR1−DNGi complexes

Lan and Pas share similar core structures, characterized by a β-turn formed by (D-Trp)−Lys motifs. While both Lan and Pas can bind to various members of the SSTR family with differing affinities, their affinity for SSTR1 is suboptimal (Fig. 1A). To investigate the binding mode of SSAs on SSTR1, we first co-expressed and purified wild-type human SSTR1, the dominant-negative form of human Gαi1 (DNGi), human Gβ1, and human Gγ2 in sf9 cells. Next, we added Lan and Pas as agonists during the protein purification step. Finally, we introduced the antibody scFv16 to stabilize the purified SSTR1−Lan/Pas−DNGi complexes.

To understand the SSTR1 activation and selectivity of Lan and Pas, we determined the cryo-EM structures of SSTR1−DNGi−scFv16 bound to agonists Lan and Pas at global resolutions of 3.37 and 2.79 Å, respectively (Table 1, Fig. 1B−G).

To investigate the conformational changes of SSTR1 induced by the ligands, a comparative analysis was conducted between the ligands-bound SSTR1 and the SSTR1−APO structures from AlphaFold. The binding of Lan to the SSTR1 orthosteric pocket triggers a series of conformational changes: the upper segment of TM2 constricts towards the receptor core, TM3 shifts downward after ligand binding, and the upper part of TM5 moves closer to TM6, while the lower part of TM5 shifts outward by 2.3 Å. Influenced by these changes in TM5, the lower half of TM6 extends outward by 12.5 Å, creating space at the bottom of SSTR1 for G protein coupling. Additionally, a slight rotation of TM7 brings the associated helix 8 closer to TM6 (Fig. 2A).

Upon Lan binding, two key residues, D137$^{3.32}$ and Y313$^{7.43}$, shift toward the ligand to form hydrophilic and salt bridge interactions (Fig. 2B). Several hydrophobic residues also rotate to create a binding pocket that accommodates Lan hydrophobic framework (Fig. 2C). During activation, residues on ECL2 and ECL3 undergo conformational changes, with N209^{ECL2} shifting closer to the hydrophilic residues of ligand compared to APO−SSTR1 (Fig. 2D). In the orthosteric pocket, Lan forms a Cys2−Cys7 disulfide bridge. D300^{ECL3} experiences dipole−dipole interactions and van der Waals forces from the disulfide bridge, causing D300^{ECL3} shift toward Lan (Fig. 2E).

Although synthetic SSAs are designed to target SSTRs for therapeutic purposes, their affinity to SSTR1 is generally lower than that of the endogenous ligand SST14. Currently, there is no available binding model of SST14 with SSTR1. Therefore, we utilized the SSTR4−SST14 (PDB 7XMT) model, which belongs to the same somatostatin receptor family 2 (SRIF2) subfamily, for

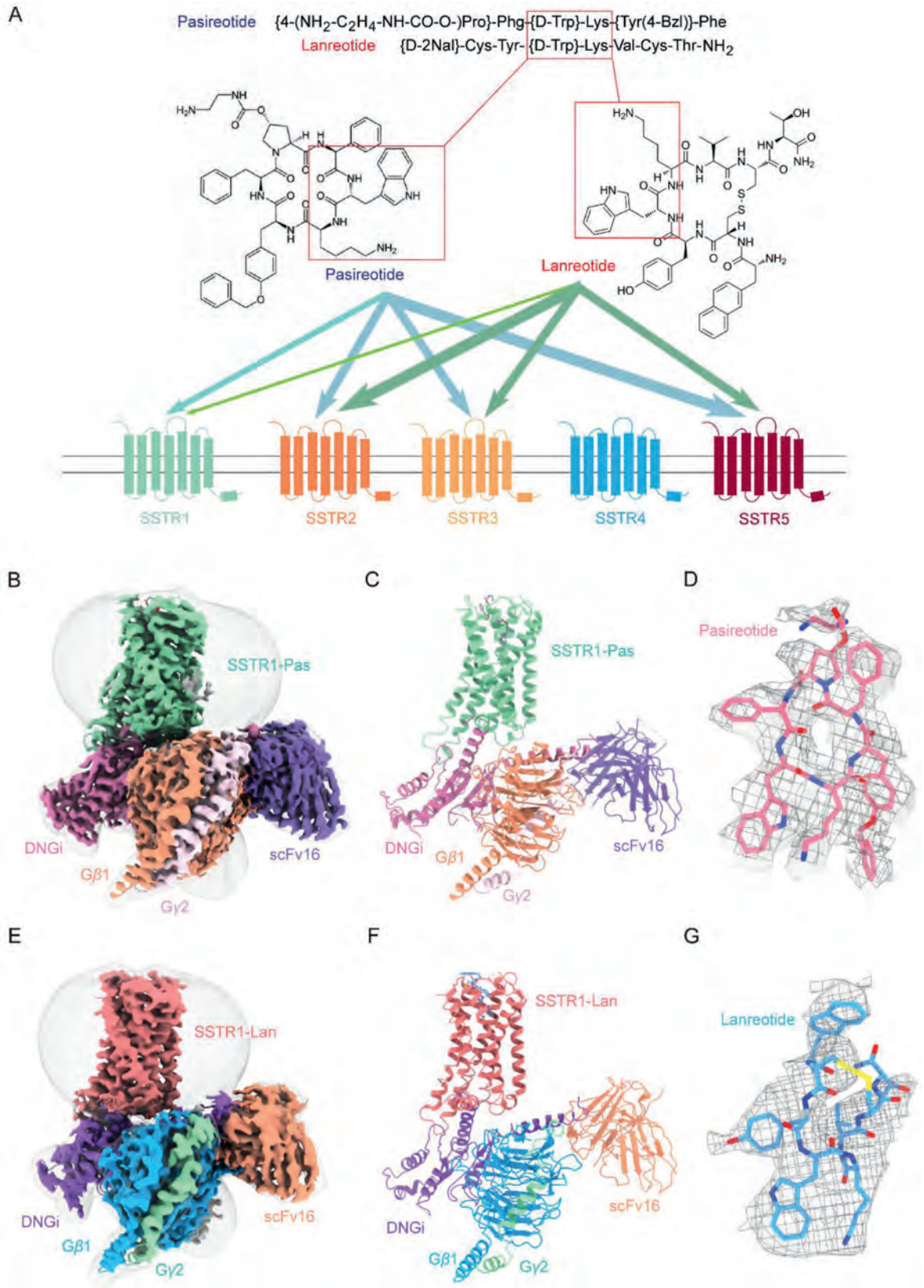

Figure 1 Structural analysis of the SSTR1−DNGi−Gβ1γ2−scFv16 complex. (A) Comparative analysis of Lan and Pas sequences and 2D structures, highlighting (D-Trp)−Lys as a key binding site that influences affinity profiles across the SSTR family. (B) Cryo-EM density maps of SSTR1−Pas. (C) Structural representation of the SSTR1−Pas complex. (D) Molecular structure of Pas (pink). (E) Cryo-EM density maps of SSTR1−Lan. (F) Structural representation of the SSTR1−Lan complex. (G) Molecular structure of Lan (blue).

Table 1 Cryo-EM data collection, refinement and validation statistics.

Data collection and processing	SSTR1−DNGi −scFv16−Pas	SSTR1−DNGi −scFv16−Lan
Magnification	105,000	105,000
Voltage (kV)	300	300
Electron exposure (e^{-}/Å)	53.50	53.6
Defocus range (μm)	−1.0 to −2.0	−1.0 to −2.0
Pixel size (Å)	0.83	0.85
Symmetry imposed	C1	C1
Initial particle images (no.)	2,969,804	2,091,230
Final particle images (no.)	722,906	217,201
Map resolution (Å)	2.79	3.37
FSC threshold	0.143	0.143
Refinement		
Model resolution (Å)	2.82	3.37
Map sharpening B factor (Å)	−86.3	−125.2
Model composition		
Nonhydrogen atoms	8418	8526
Protein residues	1110	1121
B Factors (Å)		
Protein	81.67	69.21
r.m.s deviations		
Bond lengths (Å)	0.004	0.003
Bond angles (°)	0.602	0.646
Validation		
MolProbity score	1.73	1.99
Clashscore	7.98	9.54
Ramachandran plot		
Favored (%)	95.77	92.11
Allowed (%)	4.23	7.89
Disallowed (%)	0	0

comparison. This model exhibits significant structural similarities to the SSTR1−Lan/Pas complexes obtained in our study. SST14 shares a highly similar backbone with Lan/Pas, significant differences in binding have been observed in extracellular loop 2 (ECL2) of SSTR4. Specifically, $N199^{ECL2}$ forms a stable hydrogen bond with SST14. In contrast, the corresponding residue in SSTR1, $N209^{ECL2}$, does not engage in a similar interaction with Lan or Pas. The polar interactions in ECL2 may serve as a protective mechanism, potentially preventing the premature release of SST14 upon receptor activation (Fig. 3A and B).

3.2. *Ligands recognition of SSTR1*

Determining the precise orientation of Lan in SSTR1 orthosteric pocket is challenging due to its cyclic structure. To identify the correct pose of Lan in the binding pocket, we employed molecular docking and molecular dynamic simulations (MD) to predict the pose with the highest affinity and stability.

Using the molecular docking module in Schrödinger Maestro Glide, we obtained three possible binding conformations (Supporting Information Fig. S3B, S3D, S3F, S3G). Since Glide calculations do not account for the fundamental thermodynamics of binding free energy, we further validated these 3 models using MD simulations. The best pose (Conf1) showed superior stability, with a root mean square deviation (RMSD) of 4.40 Å and the least structural deviation during the simulation period (Fig. S3A−S3F). Conf1 also showed the lowest binding free energy of −53.37 kcal/mol, which was significantly lower than the binding free energies of other poses (8.64 and −16.01 kcal/mol) (Supporting Information Figs. S3H and S4). In contrast, Pas has characteristic phenol motifs Tyr(4-Bzl) that enable precise docking of its structure into the EM map within the SSTR1 orthosteric pocket.

The orthosteric ligand pocket for Lan and Pas within SSTR1 exhibited similar conformations. The pocket is located in the transmembrane region formed by TM2−3, TM5−7, ECL2, and ECL3. Residues within 5 Å of the ligand are identified as crucial for receptor−ligand interactions. The lysine side chain nitrogen on Lan and Pas forms a salt bridge with $D137^{3.32}$ on TM3 and a hydrogen bond with $Y313^{7.43}$ on TM7 simultaneously. Hydrophobic interactions contributed by $L114^{2.60}$, $L220^{5.35}$, and $F223^{5.38}$ are also involved in stabilizing Lan/Pas in the ligand binding pocket (Fig. 4A and B).

To validate the impact of these residues in the ligand binding pocket, a Förster resonance energy transfer (FRET)-based Epac sensor was used to measure changes in cellular cAMP levels of wild-type and mutated SSTR1 constructs. To assess the significance of the shortlisted receptor−ligand interaction sites, we generated corresponding mutants and transfected them into HEK 293T cells. We examined various transfection conditions to generate transfectants with similar expression levels of SSTR1 (both wild-type and mutants) on the HEK 293T cell surface (Supporting Information Fig. S5 and Table S1).

The dose−response curves revealed that the pIC_{50} of Lan and Pas is 6.53 and 8.00, respectively (Supporting Information Fig. S6), indicating that Pas has a stronger affinity for SSTR1 than Lan. Alanine mutations at the hydrophilic residues $D137^{3.32}$ and $Y313^{7.43}$ in SSTR1 almost completely abolished cAMP inhibition induced by both Lan and Pas (Fig. 4C and E). Similarly, the alanine mutation at $F223^{5.38}$ significantly impaired SSTR1 activation by both ligands, with a more pronounced effect on Pas. Mutations at $N209^{ECL2}$ and $D300^{ECL3}$ also reduced the potency of both Lan and Pas (Fig. 4C and E).

For Lan, the $Q291^{6.55}$ mutation eliminated SSTR1 activation, while the $L114^{2.60}$ mutation resulted in an approximately 80% decrease. The $L220^{5.35}$ mutation had no impact on Lan binding strength or efficiency. For Pas, the $Q291^{6.55}$ mutation caused a two-order magnitude reduction in cAMP inhibition efficiency. The $L114^{2.60}$ mutation did not affect Pas binding, whereas the $L220^{5.35}$ mutation significantly reduced Pas activation efficiency of SSTR1 by nearly tenfold (Fig. 4D and F).

3.3. *Comparison of SSTR1/SSTR2−Lan*

Lan and Pas are pan-SSTR SSA. However, they exhibit the weakest affinity for SSTR1 compared to SSTR2, SSTR3, and SSTR5 (Fig. 1A). $M141^{3.36}$ is a conserved residue in SRIF2 (SSTR1 and SSTR4), while in SRIF1 (SSTR2, SSTR3, and SSTR5), the corresponding residue is glutamine (Q). Lan, a first-generation SSA, shows affinity for nearly all SSTR subtypes. To elucidate the differences in binding modes that result in Lan subtype selectivity, we compared its receptor−ligand interactions with SSTR1 (low affinity) and SSTR2 (high affinity) (PDB 7XAV) (Fig. 5A). Given that our primary focus is on analyzing the binding differences of Lan in SSTR1 and SSTR2, we mainly focus on the analysis of SSTR1−Lan in this section.

Trp4−Lys5 on Lan plays a critical role in receptor−ligand interactions. The nitrogen atom of the Lys side chain forms a salt bridge with $D137^{3.32}$ and a hydrogen bond with $Y313^{7.43}$ in

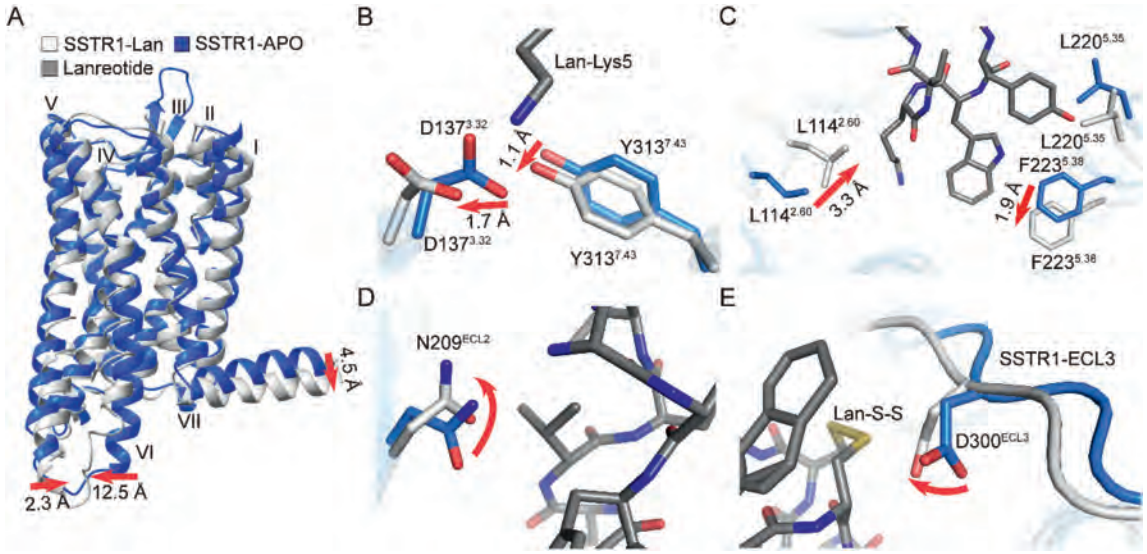

Figure 2 Comparison between SSTR1−Lan and APO−SSTR1. (A) Analysis of transmembrane helix conformational differences between the activated state of SSTR1 (white) and SSTR1−APO (blue). (B) Structural comparison of the ligand-binding pockets in SSTR1−Lan (white) and the AlphaFold-predicted inactive state of SSTR1 (blue). Upon activation by Lan (gray), the Cγ of D137$^{3.32}$ in SSTR1 shifts 1.7 Å relative to SSTR1−APO. The OH group of Y313$^{7.43}$ in SSTR1 demonstrates a 1.1 Å movement relative to SSTR1−APO. (C) Significant residue alterations involved in hydrophobic interactions following Lan binding to SSTR1. TM2 in SSTR1 transitions 3.3 Å into the receptor core, while the upper segment of TM5 shifts 1.9 Å in the direction of TM6. (D) Illustration of conformational changes in SSTR1 N209^{ECL2} before and after activation. (E) Conformational modifications in SSTR1 ECL3 and D300^{ECL3} post-activation. The positioning of ECL3 remains relatively consistent before and after activation. D300^{ECL3} reorients toward the ligand and establishes van der Waals interactions with the Lan disulfide bond.

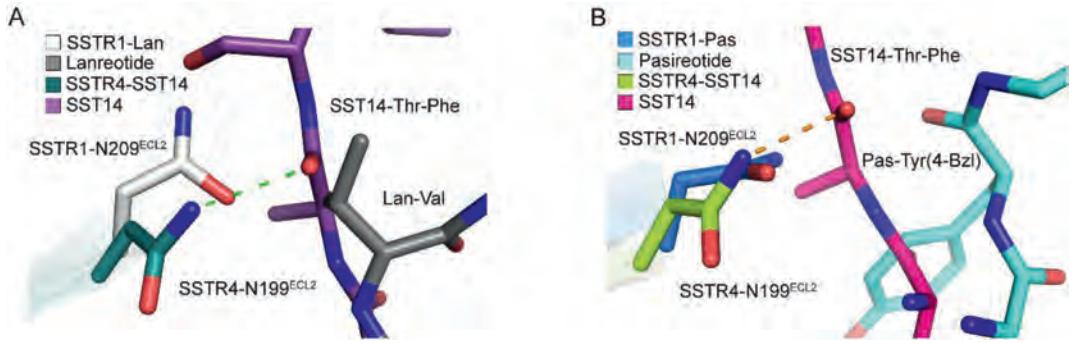

Figure 3 Comparison of ligand interactions in SSTR receptor models. (A) Comparison of N209^{ECL2} in SSTR1−Lan (white) and N199^{ECL2} in SSTR4−SST14 (dark green). N199^{ECL2} in SSTR4−SST14 forms a hydrogen bond with SST14 (purple), while N209^{ECL2} in SSTR1−Lan lacks this interaction (grey). (B) Comparison of N209^{ECL2} in SSTR1−Pas (blue) with N199^{ECL2} in SSTR4−SST14 (lemon green). N199^{ECL2} forms a hydrogen bond with SST14 (rose red), whereas N209^{ECL2} in SSTR1−Pas shows no such interaction (cyan).

SSTR1 (Fig. 5A). Moreover, the hydrophobic interaction between F$^{5.38}$ and the indole ring of Trp4 on Lan is consistently observed in both SSTR1 and SSTR2 (Fig. 5C). These interactions are characteristic of SSA binding within the SSTR1 and SSTR2.

In the SSTR2−Lan model, Q126$^{3.36}$, located deep in the binding pocket, establishes a hydrophilic interaction with Lan (Fig. 5B). This interaction is absent in our SSTR1−Lan model, which has M141$^{3.36}$ instead. Mutating M141$^{3.36}$ on SSTR1 to Q141$^{3.36}$ increased the potency for both Lan and Pas at least tenfold (Fig. 4D and F). These findings suggest that M141$^{3.36}$ is a crucial residue contributing to the subtype selectivity of the SSTR1.

In SSTR2, N276$^{6.55}$ on TM6 is a crucial residue that stabilizes Lan in the orthosteric ligand binding pocket. However, in our SSTR1 model, the corresponding residue (Q291$^{6.55}$) does not interact with the Lan (Fig. 5D). Intriguingly, our cyclic AMP assays revealed that mutating Q291$^{6.55}$ to alanine significantly reduced receptor activity in response to Lan. These findings suggest that Q291$^{6.55}$ may influence Lan-receptor interactions through indirect mechanisms.

ECL3 is thought to play a role in ligand selectivity for SSTR. Replacing SSTR2 ECL3 (Ala−Ile−Ser−Pro) with SSTR1 ECL3 completely abolishes receptor activity in response to the natural ligand SST14[24]. In our model, SSTR1's distinct ECL3 composition enables unique dipole−dipole interactions with the disulfide bridge formed by Lan itself (Fig. 5E).

3.4. Structure features of SSTR1−Lan and SSTR1−Pas

Pas was developed to address the limitations of first-generation SSAs like Lan, such as drug resistance and side effects (Fig. 1A).

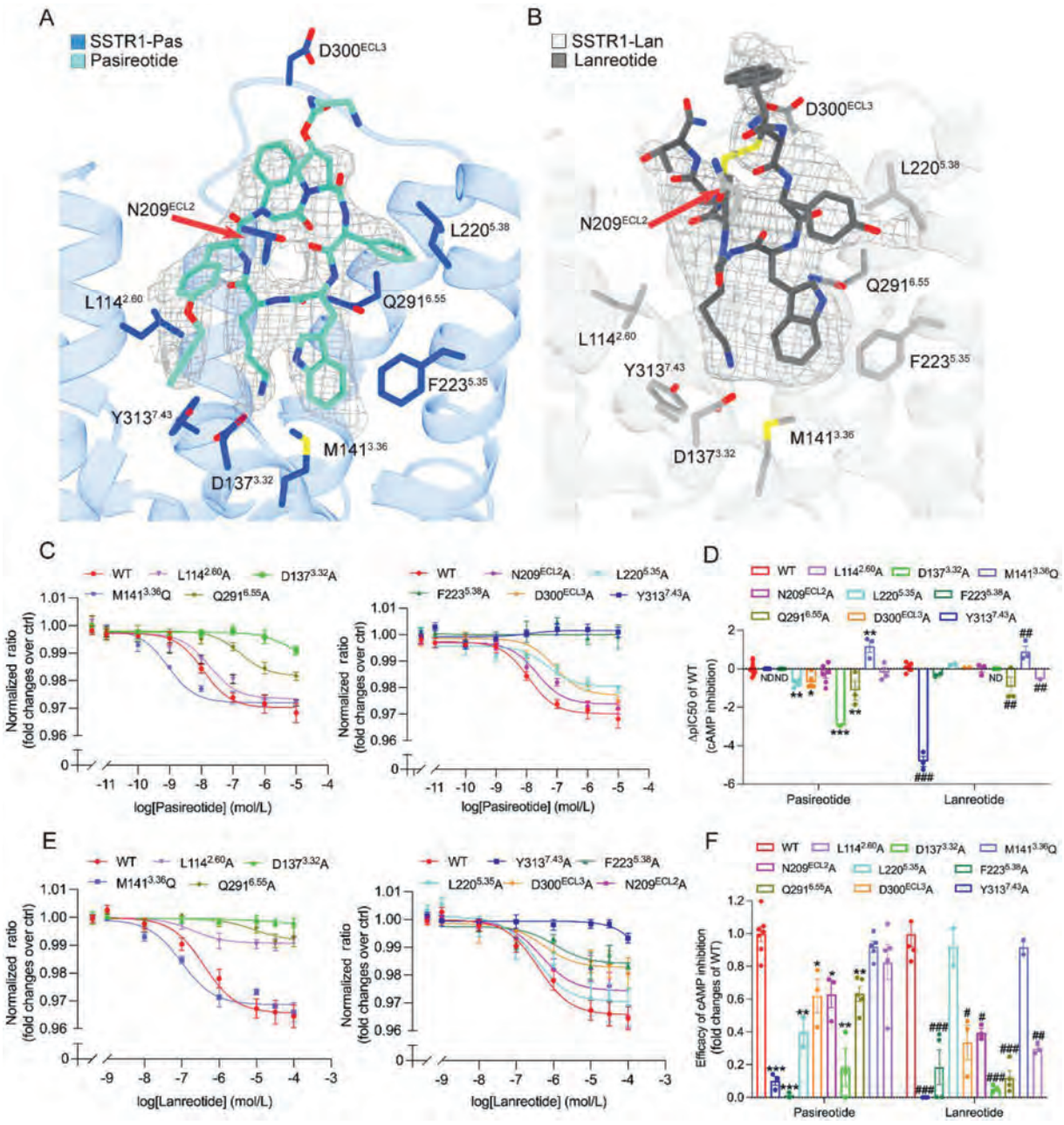

Figure 4 Analysis of cAMP responses following SSTR1 site-directed mutagenesis. (A) Schematic representation of the SSTR1−Pas ligand-binding pocket identified through cryo-EM structural analysis. (B) Detailed illustration of the SSTR1−Lan ligand-binding pocket determined *via* cryo-EM structural analysis and molecular dynamics (MD) simulations. (C), (E) Dose−response profiles demonstrating cAMP inhibition following SSTR1 activation by Pas (C) and Lan (E). (D) Quantitative assessment of calculated potency pIC_{50} values. (F) Efficacy fold changes in mutants relative to WT in cAMP inhibition assays. (For all dose−response curves, data points represent for mean ± SEM with simultaneous curve-fitting of $n = 12$ replicates. Statistical comparisons were performed with one-way or two-way analysis of variance (ANOVA). Compared to potency and efficacy of Pas bound to WT SSTR1, ND, not-determined; $^{*}P < 0.05$, $^{**}P < 0.01$, and $^{***}P < 0.001$ were considered as significantly different. Compared to potency and efficacy of Lan bound to WT SSTR1, $^{\#}P < 0.05$, $^{\#\#}P < 0.01$, and $^{\#\#\#}P < 0.001$ were considered as significantly different. The transparent bars, symbols, and error bars represent the mean, individual value, and SEM, respectively, of at least 3 independent experiments each performed in quadruplicate.

While Pas demonstrates an improved affinity for several SSTR subtypes, its affinity for SSTR1 remains suboptimal. Compared to Lan, Pas exhibits only a marginal improvement in SSTR1 potency (Fig. 6A and H, Fig. S6). The ligand pocket for Lan and Pas are similar. Key ligand-interacting residues include $D137^{3.32}$, $N209^{ECL2}$, $F223^{3.36}$, $Q291^{6.55}$, and $Y313^{7.43}$ (Fig. 6A−C, E, and G, Supporting Information Tables S2 and S3).

Hydrophobic interactions play a crucial role in stabilizing SSA within the transmembrane pocket. The hydrophobic groups of Lan and Pas interact with the hydrophobic residues within the SSTR1

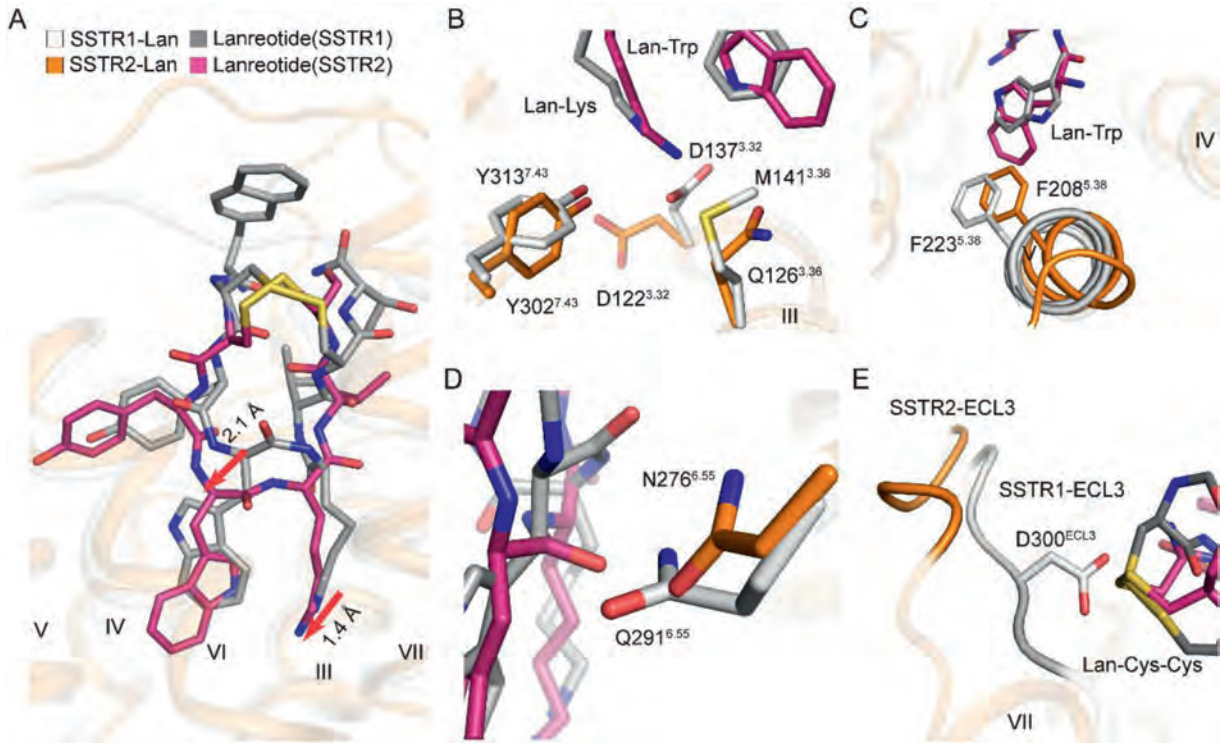

Figure 5 Comparative analysis of SSTR1−Lan and SSTR2−Lan structures. (A) Structural comparison illustrating the differential positioning of Lan when bound to SSTR1 (dark gray) *versus* SSTR2 (magenta). Lan achieves deeper penetration in the SSTR2−Lan complex compared to SSTR1−Lan, with quantifiable differences in the positioning of Trp4 Cα and the free amine of Lys5, which are situated 2.1 and 1.4 Å deeper, respectively. (B) Detailed illustration of Lan Lys5 binding interactions with SSTR1 and SSTR2 residues, demonstrating consistent interactions between the ligand and residues $D^{3.32}$ and $Y^{7.43}$ across both receptors. $M141^{3.36}$/$Q126^{3.36}$ is identified as a key determinant influencing Lan selectivity between the SRIF1 and SRIF2 subfamilies. (C) $F^{5.38}$ exhibits consistent functionality in both receptor subtypes. (D) Structural comparison of the selectivity-determining residues SSTR1−$Q291^{6.55}$ and SSTR2−$N276^{6.55}$. (E) Structural comparison of ECL3 conformations in SSTR1−Lan and SSTR2−Lan complexes.

binding pocket. For example, these interactions occur between the phenol group of $Y313^{7.43}$, the indole group of the Trp side chain, and the Lys side chains on Lan and Pas, and the residue $L114^{2.60}$ on SSTR1. Interestingly, our study shows that mutating $L114^{2.60}$ to alanine specifically affects the hydrophobic interactions of Lan with SSTR1 (Fig. 4C−F). From our SSTR1−Pas model, there is an additional hydrophobic moiety in Pas, Tyr(4-Bzl), which contributes to the stabilization of Pas in this universal ligand binding pocket (Fig. 6F).

Another significant hydrophobic interaction occurs between the phenyl ring of Phe in Pas or Tyr in Lan and $L220^{5.35}$ on TM5. Mutation of $L220^{5.35}$ on SSTR1 impacts Pas activity while leaving Lan activity unaffected (Figs. 4C−F, 6D, 6FF). We have also attempted to obtain a complex of octreotide, another first-generation SSA drug, with SSTR1. However, due to its lower potency compared to Lan, we have not yet successfully acquired structural data on the interaction between SSTR1 and octreotide (Supporting Information Fig. S7).

4. Discussion

Somatostatin analogs (SSAs) are effective drugs for cancer treatment[25,26]. While SSTR2, SSTR3, and SSTR5 readily bind SSAs, SSTR1 shows lower affinity due to its distinct transmembrane structure[27,28]. Given that SSTR1 overexpression might be associated with specific cancer types (such as prostate cancer) and have prognostic value, an in-depth understanding of how SSA interacts with SSTR1 is vital for developing more effective targeted therapies[29]. Comparative analysis of amino acid sequences across all SSTR subtypes demonstrated high conservation among SSTR family members (Supporting Information Fig. S8). Consequently, we sought to investigate the ligand-binding mechanism through structural analysis.

As a first-generation somatostatin analog (SSA), Lan effectively inhibits neuropeptide and growth hormone secretion, making it valuable for clinical interventions targeting somatostatin receptors (SSTRs). Clinical research has demonstrated the efficacy of Lan in managing both neuroendocrine and non-endocrine neoplasms[30]. In terms of receptor affinity, Lan exhibits a pronounced preference for the SRIF1 receptor family, particularly SSTR2. It displays lower potency for SSTR3 and SSTR5, while its affinity for SSTR1 is markedly reduced. Previous reports have shown that Lan's affinity for SSTR1 is substantially lower than that of the endogenous ligand SST14, with an IC_{50} value 193-fold higher[12].

Comparative results show that the ligand binding interface formed by TM3 is a crucial determinant of Lan potency. $Q126^{3.36}$ of SSTR2 corresponds to a position homologous to $M141^{3.36}$ in SSTR1. Within SSTR2, $Q126^{3.36}$ is positioned deeply in the orthosteric binding pocket, where its polar amino acid side chain

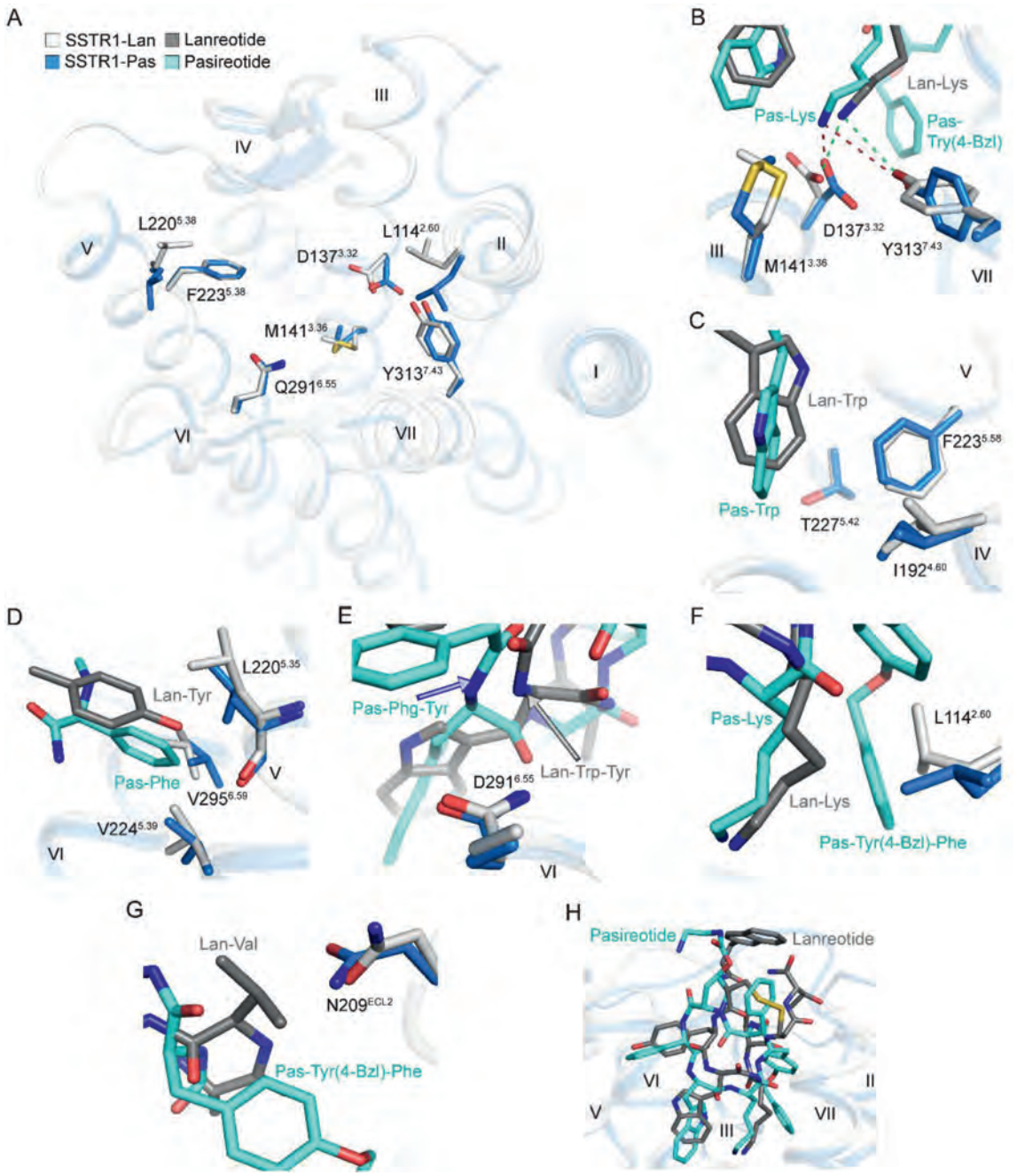

Figure 6 Comparison of SSTR1−Lan and SSTR1−Pas binding pockets. (A) This comparative analysis reveals the structural differences between SSTR1−Lan (white) and SSTR1−Pas (blue) binding pockets, with notable conformational variations in key residues: L144$^{2.60}$, D137$^{3.32}$, M141$^{3.36}$, L220$^{5.35}$, F223$^{5.38}$, Q291$^{6.55}$, and Y313$^{7.43}$. (B) Structural comparison demonstrating the positioning of residues D137$^{3.32}$, Y313$^{7.43}$, and M141$^{3.36}$ in both SSTR1−Lan and SSTR1−Pas complexes. (C) Conformational analysis of F223$^{5.38}$ across both models, illustrating how this residue creates a hydrophobic pocket that accommodates the ligands' indole moiety. (D) The diagram shows the interaction differences of residue L220$^{5.35}$ in SSTR1 with Pas and Lan, where only Pas binding is affected by this residue. (E) While D291$^{6.55}$ maintains identical conformations in both models, its functional impact is more pronounced for Lan interactions compared to Pas. (F) L144$^{2.60}$ serves as a critical residue that forms a hydrophobic pocket accommodating Lan Lys4, while primarily influencing the Tyr(4-Bzl) side chain positioning in Pas. (G) N209^{ECL2} establishes interactions with the hydrophilic functional groups of Tyr(4-Bzl)−Phe in both Pas and Lan complexes. (H) Comprehensive visualization of binding conformations for Pas (cyan) and Lan (gray).

facilitates hydrogen bond formation with Lan[31]. Conversely, in SSTR1, this polar interaction is eliminated due to the substitution of the polar residue Q126$^{3.36}$ with the hydrophobic residue M141$^{3.36}$.

N276$^{6.55}$ (SSTR2) and Q291$^{6.55}$ (SSTR1) represent another critical residue influencing Lan affinity across SSTR subtypes. Within SSTR2, polar N276$^{6.55}$ establishes stable interactions with Lan. Research has demonstrated that substitution of N276$^{6.55}$ on SSTR2 with Q276$^{6.55}$ suppressed calcium mobilization linked to SSTR2 activation[31]. Despite Q291$^{6.55}$ on SSTR1 possessing a longer polar side chain relative to its SSTR2 equivalent, our

SSTR1−Lan model did not reveal any hydrogen bond interaction involving Q291$^{6.55}$.

For both SAAs, the β-turn configuration formed by tryptophan and lysine residues appears to be an important determinant for binding affinity, with this structural motif potentially contributing to receptor−ligand interactions. Future drug development efforts might consider exploring the polar interactions between the ligand's lysine moiety and both D137$^{3.32}$ and Y313$^{7.43}$ residues. Such modifications could potentially be achieved through the introduction of functional groups that form polar interactions along the lysine side chain. Furthermore, structural adjustments of the β-turn to potentially enhance interaction with SSTR1 M141$^{3.36}$ might be worth investigating as a strategy to possibly improve overall potency.

Pas, a second-generation somatostatin analog, was developed and introduced into clinical practice[7]. Despite Pas significantly enhancing potency for SSTR1, its affinity for this receptor compared to Lan remains approximately 10-fold lower than that of the endogenous ligand somatostatin[7,12,32]. It should be noted that Pas treatment is associated with adverse events, including diabetes[33]. Pas exhibits strong binding affinity for SSTR5 receptors in pancreatic β-cells, thereby inhibiting GLP-1 secretion and consequently elevating blood glucose levels[34]. Therefore, future drug development efforts should focus on enhancing Pas binding specificity for SSTR1 while reducing its affinity for SSTR5.

In our SSTR1−Pas model, D137$^{3.32}$ again plays a pivotal role in stabilizing ligand in the orthosteric pocket of SSTR1. D137$^{3.32}$ interacts with Pas within a hydrophobic pocket formed by L114$^{2.60}$, M141$^{3.36}$, Y313$^{7.43}$, and the Trp indole group on the ligand. Notably, Tyr(4-Bzl) inserts into this pocket, occupying additional space and further stabilizing the hydrophobic pocket structure.

Based on structural comparisons between SSTR5 and SSTR1, we propose that 2 potential modifications to the "Trp−Lys" fragment of Pas might be worth exploring: extension of the Lys side chain and incorporation of aromatic groups. We hypothesize that an extended Lys side chain could potentially enhance polar interactions with D137$^{3.32}$ and Y313$^{7.43}$. Additionally, introducing an aromatic ring might facilitate Met-aromatic interactions with SSTR1 M141$^{3.36}$ while potentially strengthening $\pi-\pi$ stacking with SSTR1 F223$^{5.38}$, which might improve Pas potency toward SSTR1. In our models, the G protein-binding domains in SSTR1−Lan and SSTR1−Pas complexes revealed no substantial structural differences between these interfaces (Supporting Information Figs. S9 and S10).

5. Conclusions

In conclusion, our study has provided structural insights into the interactions between SSTR1 and two SSA, Pas and Lan. These findings could contribute to our understanding of SSTR1 activation mechanisms and ligand binding specificity. The elucidated structures offer a foundation for the rational design of next-generation SSTR1-targeted therapeutics with enhanced specificity and affinity.

Acknowledgments

We sincerely appreciate the Kobilka Cryo-Electron Microscopy Center at The Chinese University of Hong Kong (Shenzhen, China) for providing access to the cryo-electron microscopy facility. This work was supported by funds from the Ganghong Young Scholar Development Fund (China) and the Shenzhen−Hong Kong Cooperation Zone for Technology and Innovation (No. HZQB-KCZYB-2020056, China). Thiansze Wong is supported by research fundings from Shenzhen Pengcheng Peacock Plan (Nos. 2021TC0059 and 2024TC0153, China). Yang Du is supported by grants from the National Natural Science Foundation of China (No. 32271263), Shenzhen Sci. & Tech Innovation Bureau (Nos. JCYJ 20220818103009018 and JCYJ 20240813113521028, China), and the Shenzhen−Hong Kong Cooperation Zone for Technology and Innovation (No. HZQB-KCZYB-2020056, China). Richard Ye is supported by Shenzhen Medical Research Fund (No. SMRFD2403009, China), Joint Research Fund of the Second Affiliated Hospital-School of Medicine, the Chinese University of Hong Kong, Shenzhen (No. YXLH13, China), Ganghong Young Scholar Development Fund (No. 2019E0020), and Fund from Shenzhen-Hong Kong Cooperation Zone for Technology and Innovation (No. HZQB-KCZYB-2020056, China). Jing Chen is supported by the National Natural Science Foundation of China (No. 31271243).

Author contributions

Zicheng Zheng, Qiwen Liao, Shiyi Gan, Xinyu Li, Tiantian Xiong, Lezhi Xu, Dan Li, and Yunlu Jiang performed the experiment, data collection, model building, and manuscript preparation. Zicheng Zheng, Thiansze Wong and Tiantian Xiong, contributed to the writing and figure/table preparation. Thiansze Wong, Yang Du, Richard Ye and Jing Chen supervised the project and revised the manuscript. All authors contributed to the article. All authors have read and approved the final version of the manuscript.

Conflicts of interest

The authors declare no competing interests.

Appendix A. Supporting information

Supporting information to this article can be found online at https://doi.org/10.1016/j.apsb.2025.03.043.

References

1. Francis BH, Baskin DG, Saunders DR, Ensinck JW. Distribution of somatostatin-14 and somatostatin-28 gastrointestinal-pancreatic cells of rats and humans. *Gastroenterology* 1990;**99**:1283−91.
2. Bodart G, Farhat K, Charlet-Renard C, Salvatori R, Geenen V, Martens H. The somatotrope growth hormone-releasing hormone/-growth hormone/insulin-like growth factor-1 axis in immunoregulation and immunosenescence. *Front Horm Res* 2017;**48**:147−59.
3. Pages P, Benali N, Saint-Laurent N, Esteve JP, Schally AV, Tkaczuk J, et al. sst2 somatostatin receptor mediates cell cycle arrest and induction of p27(Kip1). Evidence for the role of SHP-1. *J Biol Chem* 1999;**274**:15186−93.
4. Ferjoux G, Lopez F, Esteve JP, Ferrand A, Vivier E, Vely F, et al. Critical role of Src and SHP-2 in sst2 somatostatin receptor-mediated activation of SHP-1 and inhibition of cell proliferation. *Mol Biol Cell* 2003;**14**: 3911−28.
5. Gunther T, Tulipano G, Dournaud P, Bousquet C, Csaba Z, Kreienkamp HJ, et al. International union of basic and clinical pharmacology. CV. somatostatin receptors: structure, function, ligands, and new nomenclature. *Pharmacol Rev* 2018;**70**:763−835.
6. Mayo KE, Godfrey PA, Suhr ST, Kulik DJ, Rahal JO. Growth hormone-releasing hormone: synthesis and signaling. *Recent Prog Horm Res* 1995;**50**:35−73.

7. Vitale G, Dicitore A, Sciammarella C, Di Molfetta S, Rubino M, Faggiano A, et al. Pasireotide in the treatment of neuroendocrine tumors: a review of the literature. *Endocr Relat Cancer* 2018;**25**:R351−64.
8. Baldelli R, Barnabei A, Rizza L, Isidori AM, Rota F, Di Giacinto P, et al. Somatostatin analogs therapy in gastroenteropancreatic neuroendocrine tumors: current aspects and new perspectives. *Front Endocrinol* 2014;**5**:7.
9. Ionovici N, Carsote M, Terzea DC, Predescu AM, Rauten AM, Popescu M. Somatostatin receptors in normal and acromegalic somatotroph cells: the U-turn of the clinician to immunohistochemistry report—a review. *Rom J Morphol Embryol* 2020;**61**:353−9.
10. Feelders RA, Yasothan U, Kirkpatrick P. Pasireotide. *Nat Rev Drug Discov* 2012;**11**:597−8.
11. Reubi JC, Schaer JC, Waser B, Hoeger C, Rivier J. A selective analog for the somatostatin sst1-receptor subtype expressed by human tumors. *Eur J Pharmacol* 1998;**345**:103−10.
12. Gut P, Waligorska-Stachura J, Czarnywojtek A, Sawicka-Gutaj N, Baczyk M, Ziemnicka K, et al. Management of the hormonal syndrome of neuroendocrine tumors. *Arch Med Sci* 2017;**13**:515−24.
13. Jo S, Kim T, Iyer VG, Im W. CHARMM-GUI: a web-based graphical user interface for CHARMM. *J Comput Chem* 2008;**29**:1859−65.
14. Lomize MA, Pogozheva ID, Joo H, Mosberg HI, Lomize AL. OPM database and PPM web server: resources for positioning of proteins in membranes. *Nucleic Acids Res* 2012;**40**:D370−6.
15. Huang J, MacKerell Jr AD. CHARMM36 all-atom additive protein force field: validation based on comparison to NMR data. *J Comput Chem* 2013;**34**:2135−45.
16. Vanommeslaeghe K, Hatcher E, Acharya C, Kundu S, Zhong S, Shim J, et al. CHARMM general force field: a force field for drug-like molecules compatible with the CHARMM all-atom additive biological force fields. *J Comput Chem* 2010;**31**:671−90.
17. Abraham MJ, Murtola T, Schulz R, Páll S, Smith JC, Hess B, et al. GROMACS: high performance molecular simulations through multi-level parallelism from laptops to supercomputers. *SoftwareX* 2015;**1−2**:19−25.
18. Darden T, York D, Pedersen L. Particle mesh Ewald: an N•log(N) method for Ewald sums in large systems. *J Chem Phys* 1993;**98**:10089−92.
19. Hess B, Bekker H, Berendsen HJC, Fraaije JGEM. LINCS: a linear constraint solver for molecular simulations. *J Comput Chem* 1997;**18**:1463−72.
20. Michaud-Agrawal N, Denning EJ, Woolf TB, Beckstein O. MDAnalysis: a toolkit for the analysis of molecular dynamics simulations. *J Comput Chem* 2011;**32**:2319−27.
21. Valdes-Tresanco MS, Valdes-Tresanco ME, Valiente PA, Moreno E. gmx_MMPBSA: a new tool to perform end-state free energy calculations with GROMACS. *J Comput Chem* 2021;**17**:6281−91.
22. Storch U, Straub J, Erdogmus S, Gudermann T, Mederos YSM. Dynamic monitoring of $G_{i/o}$-protein-mediated decreases of intracellular cAMP by FRET-based Epac sensors. *Pflügers Archiv* 2017;**469**:725−37.
23. Klarenbeek J, Goedhart J, van Batenburg A, Groenewald D, Jalink K. Fourth-generation epac-based FRET sensors for cAMP feature exceptional brightness, photostability and dynamic range: characterization of dedicated sensors for FLIM, for ratiometry and with high affinity. *PLoS One* 2015;**10**:e0122513.
24. Robertson MJ, Meyerowitz JG, Panova O, Borrelli K, Skiniotis G. Plasticity in ligand recognition at somatostatin receptors. *Nat Struct Mol Biol* 2022;**29**:210−7.
25. Florio T. Somatostatin/somatostatin receptor signalling: phosphotyrosine phosphatases. *Mol Cell Endocrinol* 2008;**286**:40−8.
26. Hofland LJ, Lamberts SW. Somatostatin receptors and disease: role of receptor subtypes. *Baillieres Clin Endocrinol Metab* 1996;**10**:163−76.
27. Modarai SR, Opdenaker LM, Viswanathan V, Fields JZ, Boman BM. Somatostatin signaling *via* SSTR1 contributes to the quiescence of colon cancer stem cells. *BMC Cancer* 2016;**16**:941.
28. Li M, Wang X, Li W, Li F, Yang H, Wang H, et al. Somatostatin receptor-1 induces cell cycle arrest and inhibits tumor growth in pancreatic cancer. *Cancer Sci* 2008;**99**:2218−23.
29. Pedraza-Arevalo S, Hormaechea-Agulla D, Gomez-Gomez E, Requena MJ, Selth LA, Gahete MD, et al. Somatostatin receptor subtype 1 as a potential diagnostic marker and therapeutic target in prostate cancer. *Prostate* 2017;**77**:1499−511.
30. Theodoropoulou M, Stalla GK. Somatostatin receptors: from signaling to clinical practice. *Front Neuroendocrinol* 2013;**34**:228−52.
31. Bo Q, Yang F, Li Y, Meng X, Zhang H, Zhou Y, et al. Structural insights into the activation of somatostatin receptor 2 by cyclic SST analogues. *Cell Discov* 2022;**8**:47.
32. Wolin EM, Jarzab B, Eriksson B, Walter T, Toumpanakis C, Morse MA, et al. Phase III study of pasireotide long-acting release in patients with metastatic neuroendocrine tumors and carcinoid symptoms refractory to available somatostatin analogues. *Drug Des Dev Ther* 2015;**9**:5075−86.
33. Samson SL. Pasireotide in acromegaly: an overview of current mechanistic and clinical data. *Neuroendocrinology* 2015;**102**:8−17.
34. Chisholm C, Greenberg GR. Somatostatin-28 regulates GLP-1 secretion *via* somatostatin receptor subtype 5 in rat intestinal cultures. *Am J Physiol Endocrinol Metab* 2002;**283**:E311−7.